

TAPM-Net: Trajectory-Aware Perturbation Modeling for Infrared Small Target Detection

Hongyang Xie

Hongyang.Xie@warwick.ac.uk

Hongyang He

Hongyang.He@warwick.ac.uk

Victor Sanchez

v.f.sanchez-silva@warwick.ac.uk

Signal and Information Processing

(SIP) Lab

The University of Warwick

Coventry, UK

Abstract

Infrared small target detection (ISTD) remains a long-standing challenge due to weak signal contrast, limited spatial extent, and cluttered backgrounds. Despite performance improvements from convolutional neural networks (CNNs) and Vision Transformers (ViTs), current models lack the mechanism to trace how small targets trigger directional, layer-wise perturbations in the feature space—an essential cue for distinguishing signal from structured noise in infrared scenes. To address this limitation, we propose the Trajectory-Aware Mamba Propagation Network (TAPM-Net) that explicitly models the spatial diffusion behavior of target-induced feature disturbances. TAPM-Net is built upon two novel components: a Perturbation-guided Path Module (PGM) module and a Trajectory-Aware State Block (TASB). The PGM module constructs perturbation energy fields from multi-level features and extracts gradient-following feature trajectories that reflect the directionality of local responses. The resulting feature trajectories are fed into the TASB, which is a Mamba-based state-space unit that models dynamic propagation along each trajectory while incorporating velocity-constrained diffusion and semantic-aligned feature fusion from word- and sentence-level embeddings. Unlike existing attention-based methods, TAPM-Net enables anisotropic, context-sensitive state transitions along spatial trajectories, maintaining global coherence at low computational cost. Experiments on NUAA-SIRST and IRSTD-1K demonstrate that TAPM-Net achieves SOTA performance in ISTD.

Introduction

Infrared small target detection (ISTD) is a crucial task in surveillance, remote sensing, and defense applications. Traditional approaches for ISTD predominantly focus on background suppression [1, 2, 3, 4], and low-rank [5, 6] and sparse decomposition techniques [7, 8, 9]. These approaches aim to isolate targets by modeling the background as a low-rank structure while treating the targets as sparse outliers. However, they often suffer from low detection accuracy, poor generalization to complex scenes, and vulnerability to structured noise.

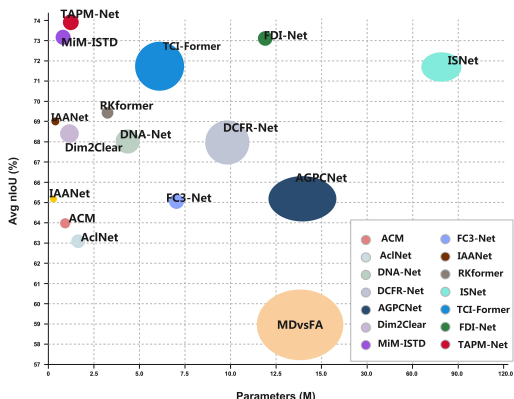


Figure 1: Performance vs. complexity of several models on the NUAA-SIRST dataset. Each model is represented by a distinct color. The size of each marker reflects the relative computational cost of the corresponding model.

constrained applications. Moreover, they lack an explicit mechanism to trace how feature disturbances propagate spatially, especially when such disturbances are weak or distributed.

To address these limitations, we draw inspiration from physical diffusion models [9, 10, 11, 12, 13] and propose a fundamentally different approach: treating small targets not as isolated saliency peaks but as sources of structured perturbation that propagate through the feature space. We then introduce TAPM-Net, a Trajectory-Aware Mamba Propagation Network that models the spatial dynamics of target-induced disturbances in a principled and learnable manner. TAPM-Net comprises two key modules: the Perturbation-guided Path Module (PGM), which constructs energy fields from backbone features and extracts gradient-aligned propagation feature trajectories; and the Trajectory-Aware State Block (TASB), which uses the Mamba architecture to recursively model state transitions along each trajectory. This design enables efficient, directional, and semantically aligned propagation modeling with low computational overhead. Unlike attention-based models that operate globally and uniformly, TAPM-Net focuses on structured, trajectory-aware propagation, thus capturing not only where the target is, but how its influence spreads. As shown in Figure 1, TAPM-Net outperforms existing methods in both accuracy and efficiency by fully leveraging data-driven spatial propagation. Instead of relying on handcrafted priors, TAPM-Net learns perturbation-aware feature trajectories directly from feature distributions and models them efficiently using a Mamba-based state-space formulation. Our contributions are then threefold:

- Our work is the first to introduce a perturbation-based formulation into the ISTD task, modeling small targets as localized disturbance sources and constructing energy fields to trace their spatial influence.
- Inspired by physical diffusion, we design a trajectory-aware state-space modeling framework built on Mamba, enabling efficient and semantically aligned feature propagation along gradient-guided trajectories.

By learning data-driven discriminative features, CNN-based methods [8, 10, 11, 12, 13, 14, 15, 16, 17, 18, 19, 20, 21, 22, 23, 24] outperform traditional ISTD methods in both precision and recall. However, many of these methods still rely on local contrast cues or global saliency estimation, and thus struggle to maintain fine-grained sensitivity to subtle, dispersed targets, particularly in highly textured or dynamic environments. Recently, ViTs [25] and hybrid CNN-Transformer architectures [8, 10, 11] have further pushed detection accuracy by leveraging global self-attention and cross-layer fusion. Despite their strong performance, these models are typically computationally expensive, making them impractical for resource-

- TAPM-Net achieves superior accuracy and computational efficiency in the NUAA-SIRST and IRSTD-1K datasets, confirming its effectiveness under both detection and deployment constraints.

2 Related work

ISTD networks. Recent advances in ISTD have been driven by deep learning models, particularly CNNs, evaluated on the NUAA-SIRST [9] benchmark, first introduced by ACM [2] to promote standardized evaluation. For example, MDvsFA [79] proposes feature aggregation to balance false alarms and miss-detections. DNANet [10] introduces dense nested connections for multi-scale context modeling, while UIUNet [84] leverages a U-Net to enhance spatial detail preservation. However, CNN-based methods typically focus on local feature extraction, often struggling to model weak target responses under strong background interference or to capture global context dependencies. To address these limitations, transformer-based and hybrid models have emerged. For example, TCI-Former [8] introduces target-contour interaction to jointly model target structures and their surrounding context, improving boundary preservation. MiM-ISTD [8] proposes a nested Mamba-in-Mamba architecture to model feature perturbation propagation across scales, enhancing robustness in complex scenes. These methods partially bridge local-global feature integration but remain computationally demanding.

Despite recent advances, ISTD still faces long-term challenges in robustly modeling weak, structureless targets in cluttered environments while maintaining computational efficiency. Motivated by these gaps, our proposed TAPM-Net introduces trajectory-guided feature modeling and Mamba-based state propagation, enabling efficient disturbance-aware detection with enhanced spatial coherence and long-range dependency modeling.

State-space sequence modeling in vision tasks. These models emerge as efficient alternatives to self-attention mechanisms to capture long-range dependencies in vision tasks. For example, U-Mamba [70] extends Mamba to dense pixel-wise prediction by embedding state transitions into a U-Net, improving spatial detail retention. Swin-UNet [2] integrates shifted window mechanisms with hierarchical U-Net decoding, enhancing local-global feature alignment. Weak-Mamba-U-Net [81] introduces lightweight state updates to reduce computational overhead while preserving temporal dynamics. LocalVMamba [16] constrains state propagation within local regions, improving locality awareness but limiting global context modeling. MS-VMamba [26] extends Mamba to multi-scale feature processing, enabling cross-scale dependency learning. GroupMamba [75] further decomposes state transitions into grouped channels, improving efficiency in large-scale vision tasks. While these designs demonstrate the versatility of state-space modeling, they often rely on spatially uniform token propagation, lacking physically grounded mechanisms to guide feature flows based on disturbance structures. Mamba’s linear-time recurrence offers clear advantages over attention mechanisms in terms of scalability and efficiency, but current formulations treat all spatial positions equally, ignoring localized perturbation dynamics critical to ISTD. To address this, TAPM-Net integrates trajectory-guided state propagation into the Mamba framework, enabling disturbance-aware modeling that explicitly captures anisotropic feature flow patterns induced by small targets, without sacrificing computational efficiency.

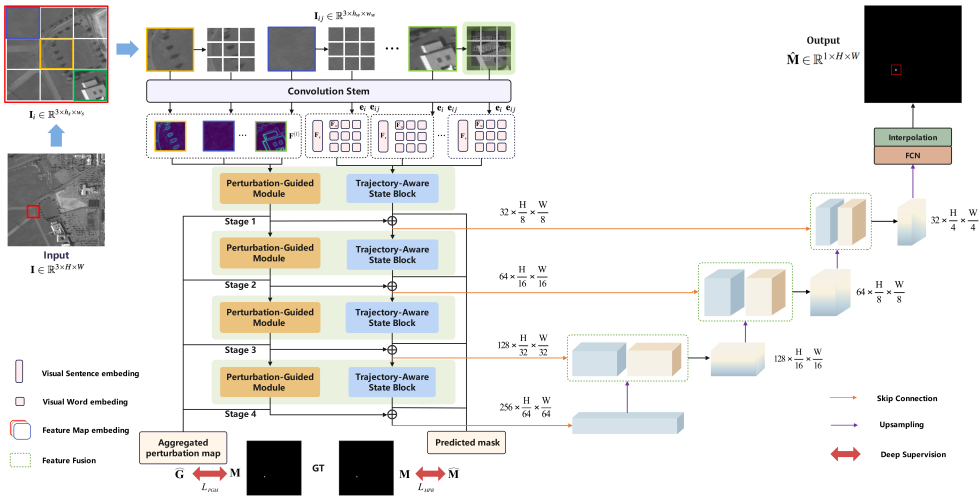


Figure 2: TAPM-Net architecture. It consists of a convolutional stem that extracts visual sentence and word embeddings, followed by multi-stage PGM and TASB for feature enhancement. Multi-scale features are fused through skip connections and upsampled during decoding to produce the final detection mask.

3 Proposed method

TAPM-Net is an ISTD solution that integrates a U-Net encoder-decoder with Mamba-based state-space modeling. As shown in Figure 2, its architecture consists of two key components: hierarchical visual feature modeling, i.e., the PGM, and the TASB. TAPM-Net first segments the input image into multi-level visual regions to capture both local and contextual information. These features are encoded using a Mamba-based multi-scale encoder, followed by perturbation-aware trajectory extraction based on local energy fields. The extracted feature trajectories are then dynamically modeled and aligned using state-space mechanisms. Finally, the decoder computes the final prediction in the form of a mask.

Given an input image $\mathbf{I} \in \mathbb{R}^{3 \times H \times W}$, TAPM-Net first divides it into n non-overlapping regions, each denoted by $\mathbf{I}_i \in \mathbb{R}^{3 \times h_s \times w_s}$. These regions are called visual sentences, with $h_s = H/\sqrt{n}$ and $w_s = W/\sqrt{n}$. Each sentence is further divided into m sub-patches, termed visual words, each denoted by $\mathbf{I}_{ij} \in \mathbb{R}^{3 \times h_w \times w_w}$, where $h_w = h_s/\sqrt{m}$ and $w_w = w_s/\sqrt{m}$. A lightweight convolutional stem (3×3 Conv, BatchNorm, GELU) extracts word embeddings, each denoted by $\mathbf{e}_{ij} \in \mathbb{R}^{C_w}$, which are aggregated into word-level features, $\mathbf{F}_w \in \mathbb{R}^{n \times m \times C_w}$. Sentence-level embeddings, each denoted by $\mathbf{e}_i \in \mathbb{R}^{C_s}$, are computed by pooling word features, forming $\mathbf{F}_s \in \mathbb{R}^{n \times C_s}$. This hierarchical representation provides a semantic basis for the subsequent perturbation and trajectory modeling stages.

PGM. As shown in Figure 3 (a), at each stage $l \in [1, 2, 3, 4]$, the backbone feature map, $\mathbf{F}^{(l)} \in \mathbb{R}^{C_l \times H_l \times W_l}$, is passed to the PGM. The feature map $\mathbf{F}^{(l)}$, constructed by a sequence of Mamba blocks, encodes rich semantic representations while retaining sufficient spatial resolution for precise localization of small objects. To explicitly characterize local disturbances potentially caused by small targets, we construct scalar-valued perturbation energy maps, each denoted by $\mathcal{E}^{(l)} \in \mathbb{R}^{H_l \times W_l}$. These maps are computed by estimating spatial gradients across the feature channels and accumulating the magnitude of changes at each location.

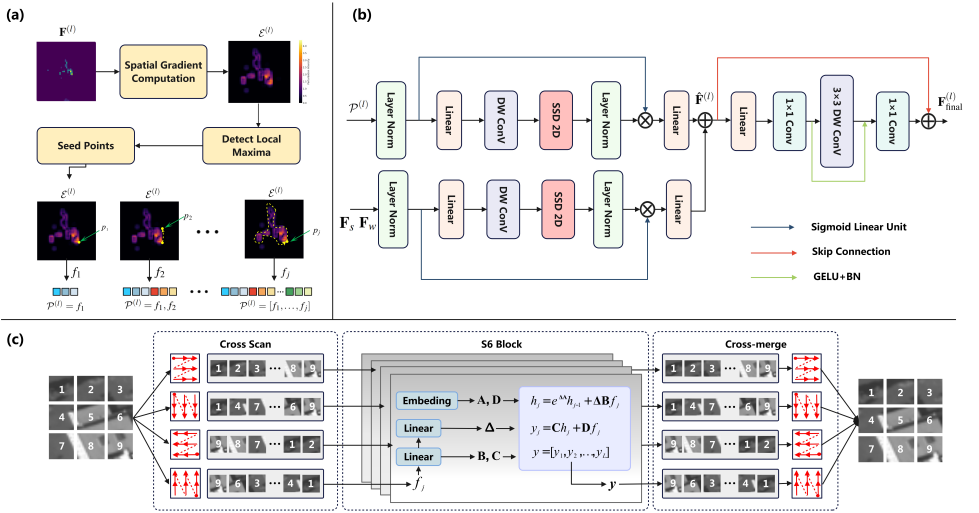


Figure 3: (a) PGM extracts trajectories from spatial energy maps. (b) TASB models feature dynamics along trajectories. (c) The SS2D block enhances spatial dependency through cross-scan and cross-merge operations.

Specifically, the energy at each position (x, y) is computed as:

$$\mathcal{E}^{(l)}(x, y) = \sum_{c=1}^{C_l} \left| \mathbf{F}_c^{(l)}(x+1, y) - \mathbf{F}_c^{(l)}(x-1, y) \right| + \left| \mathbf{F}_c^{(l)}(x, y+1) - \mathbf{F}_c^{(l)}(x, y-1) \right|, \quad (1)$$

where $\mathbf{F}_c^{(l)}$ denotes the c -th channel slice of $\mathbf{F}^{(l)}$. This operation aggregates directional differences across channels, highlighting locations with strong spatial discontinuities such as edges or localized perturbations, often associated with the presence of the target.

We initiate trajectory sampling from local maxima in each energy map, $\mathcal{E}^{(l)}$. Starting from a seed point $p_1 \in \mathbb{R}^2$, we follow the direction of steepest gradient to generate a trajectory of sampled positions. The trajectory is recursively updated by:

$$p_{j+1} = p_j + \eta \cdot \frac{\nabla \mathcal{E}^{(l)}(p_j)}{\|\nabla \mathcal{E}^{(l)}(p_j)\|_2 + \epsilon}, \quad (2)$$

where η is a step-size factor controlling the spatial resolution of the trace, and ϵ is a small constant for numerical stability. The gradient $\nabla \mathcal{E}^{(l)}$ is computed via finite differences or Sobel filters. The length of each trajectory, denoted by L , can be either fixed or adaptively determined based on the energy decay. Each point p_j along the trajectory is mapped back to the backbone feature space. Using bilinear interpolation, we extract channel-wise feature vectors; specifically, the sampled positions $\{p_j\}$ along the traced perturbation trajectory on the energy map $\mathcal{E}^{(l)}$ are used to form a sequence of feature tokens:

$$f_j = \text{Interp}(\mathbf{F}^{(l)}, p_j), \quad \mathcal{P}^{(l)} = [f_1, f_2, \dots, f_L] \in \mathbb{R}^{L \times C_l}, \quad (3)$$

where $f_j \in \mathbb{R}^{C_l}$ represents the local feature at point p_j and $\text{Interp}(\cdot, \cdot)$ denotes bilinear interpolation. The resulting sequence $\mathcal{P}^{(l)}$ encodes the spatial dynamics of perturbation propagation and serves as input to the subsequent Mamba-based trajectory modeling module.

TASB. This block models the spatial propagation of perturbation patterns induced by small targets and aligns these dynamics with global context. As shown in Figure 3(b) and (c), TASB is built on a Mamba-based Selective State-Space 2D Block (SS2D), here instantiated as the S6 Block. The S6 Block first applies cross-scan operations to unfold spatial features into directional sequences, models their sequential dependencies using a state-space update mechanism, and then recombines them via cross-merge operations to restore the spatial layout.

Starting with the sequence $\mathcal{P}^{(l)} = [f_1, \dots, f_L]$, TASB applies a state-space model to recursively update the hidden states. The update is formulated as:

$$h_j = e^{\Delta \mathbf{A}} h_{j-1} + \Delta \mathbf{B} f_j; \quad y_j = \mathbf{C} h_j + \mathbf{D} f_j; \quad y = [y_1, y_2, \dots, y_j], \quad (4)$$

where h_j represents the hidden state at step j , y_j denotes the corresponding output, y is the collection of all state outputs along the entire trajectory or sequence, \mathbf{A} is the state transition matrix that controls how the hidden state evolves over the sequence, \mathbf{B} projects feature f_j into the state update, \mathbf{C} maps the updated hidden state to the output space, \mathbf{D} allows for a direct contribution of the input feature to the output, and Δ is a learnable step-size parameter that regulates the dynamics of the update.

SS2D includes a bottleneck structure, which first reduces the channel dimension using a 1×1 linear layer before the state update, and then restores the original dimension after the update. This design improves computational efficiency while preserving feature representation capacity. To enhance spatial modeling, TASB adopts a cross-scanning strategy, where the feature map $\hat{\mathbf{F}}^{(l)}$ [see Figure 3(b)] is unfolded into four directional sequences: horizontal, vertical, diagonal, and anti-diagonal. These sequences are processed independently and merged back to restore the spatial layout.

After state modeling, TASB aligns the state output y_j with the corresponding feature f_j , word-level feature $\mathbf{F}_w(x_j, y_j)$, and sentence-level feature $\mathbf{F}_s(x_j, y_j)$. The aligned feature is computed by concatenation followed by a linear projection, $\phi(\cdot)$:

$$\mathbf{z}_j = \phi([y_j || f_j || \mathbf{F}_w(x_j, y_j) || \mathbf{F}_s(x_j, y_j)]). \quad (5)$$

TASB projects \mathbf{z}_j ; i.e., the aligned trajectory states, back to their original spatial positions (x_j, y_j) on the feature map $\hat{\mathbf{F}}^{(l)}$. When multiple states map to the same location, they are averaged by dividing by the number of contributions, $N(x, y)$. The resulting aggregated feature map $\hat{\mathbf{F}}^{(l)}$ is then fused with the original backbone feature $\mathbf{F}^{(l)}$ through residual addition, scaled by a fusion weight λ to control the contribution of the trajectory-aware features. This multi-scale fusion process ensures that spatial details, semantic alignment, and perturbation dynamics are jointly captured and progressively enhanced across the feature hierarchy.

Decoding and multi-scale feature fusion. After the multi-stage feature enhancement, the fused feature map $\mathbf{F}_{\text{final}}^{(l)}$ is the trajectory-enhanced feature map obtained by fusing $\mathbf{F}^{(l)}$ with the TASB-enhanced map $\hat{\mathbf{F}}^{(l)}$ [see Figure 3(b)]:

$$\mathbf{F}_{\text{final}}^{(l)} = \mathbf{F}^{(l)} + \lambda \cdot \hat{\mathbf{F}}^{(l)}. \quad (6)$$

The decoder contains three upsampling stages, where each stage performs bilinear interpolation followed by a 3×3 convolution, BatchNorm, and ReLU activation. The feature channels are gradually reduced from 256 to 32 (see Figure 2). At each stage, skip connections concatenate the corresponding encoder features. Finally, a fully convolutional network (FCN)

head projects the decoded features to a single-channel prediction, $\hat{\mathbf{M}} \in \mathbb{R}^{1 \times H \times W}$, followed by interpolation to match the original image size.

Loss function. TAPM-Net is optimized with a dual-branch loss. The main segmentation loss combines binary cross-entropy (BCE) and Dice loss: $\mathcal{L}_{\text{seg}} = \text{BCE}(\hat{\mathbf{M}}, \mathbf{M}) + \alpha \cdot \text{Dice}(\hat{\mathbf{M}}, \mathbf{M})$, where $\hat{\mathbf{M}}$ is the predicted mask, \mathbf{M} is the ground truth, and α balances the two terms. To guide learning, we aggregate all feature trajectorys back to their spatial locations, forming a perturbation response map $\hat{\mathbf{G}} \in \mathbb{R}^{H \times W}$. This map highlights regions influenced by perturbation flows and is used as auxiliary: $\mathcal{L}_{\text{PGM}} = \text{BCE}(\hat{\mathbf{G}}, \mathbf{M})$. The total training objective is formulated as:

$$\mathcal{L}_{\text{total}} = \mathcal{L}_{\text{seg}} + \beta \cdot \mathcal{L}_{\text{PGM}}, \quad (7)$$

where β controls the contribution of the auxiliary perturbation supervision. This loss design ensures both accurate boundary prediction and spatial consistency.

4 Performance evaluation

Datasets. We conduct experiments on two widely used ISTD datasets: NUAA-SIRST [3] and IRSTD-1k [42]. The NUAA-SIRST dataset contains 427 infrared images captured under diverse scenes, backgrounds, and target scales, providing rich variability for robust evaluation. The IRSTD-1k dataset includes 1000 images with a resolution of 512×512 pixels, covering challenging scenarios such as cluttered backgrounds, low signal-to-noise ratios, and small targets. Following standard practice, we randomly split each dataset into 80% for training and 20% for testing.

Evaluation Metrics. We adopt both pixel-level and object-level metrics, consistent with standard ISTD benchmarks. Pixel-level metrics include Intersection over Union (IoU) and Normalized IoU (nIoU), which measure spatial overlap quality. IoU evaluates the ratio between the intersection and union of predicted and ground truth masks, while nIoU mitigates scale sensitivity across different target sizes. Object-level metrics include the Probability of Detection (P_d) and False Alarm Rate (F_a).

Quantitative comparisons. We compare TAPM-Net with traditional, CNN-based, ViT-based, and hybrid methods as tabulated in Table 1. For pixel-level metrics (IoU and nIoU), hybrid methods outperform traditional methods, but many still struggle with predicting precise boundaries for small targets. TAPM-Net achieves the best scores by leveraging perturbation-guided and trajectory-aware modeling. For object-level metrics (P_d and F_a), TAPM-Net balances detection and false alarms better than others, achieving perfect detection with low false alarms on NUAA-SIRST and maintaining strong performance on IRSTD-1k, thus showing superior robustness in challenging infrared scenarios.

Figure 4 shows the true positive rate (TPR) and false positive rate (FPR) on NUAA-SIRST and IRSTD-1k. Hybrid models consistently achieve higher TPR at lower FPR compared to traditional approaches like ACM, demonstrating better sensitivity and false alarm control across both datasets. These results confirm the effectiveness of hybrid models for practical ISTD.

Visualization of results. Figure 5 depicts visual results obtained by different methods. These results cover various scenarios such as background clutter, occlusion, and the presence of similar distracting objects. It can be observed that several methods tend to produce false alarms or miss targets in challenging cases. This highlights the inherent challenges of ISTD, particularly when targets are small, with low-contrast, or surrounded by confusing background structures.

Table 1: Performance of several methods on NUAA-SIRST and IRSTD-1k. Results in **red, **orange**, and **yellow** indicate, respectively, the best, second best, and third best performance.**

Method	Type	NUAA-SIRST					IRSTD-1k		
		IoU(%)↑	nIoU(%)↑	Pd(%)↑	Fa(%)↓	IoU(%)↑	nIoU(%)↑	Pd(%)↑	Fa(%)↓
PSTNN [20]	Trad	22.40	22.35	77.95	29.11	24.57	17.93	71.99	35.26
MSLSTIPT [20]	Trad	10.30	9.58	82.13	11.31	11.43	5.93	79.03	15.24
NRAM [20]	Trad	12.16	10.22	74.52	13.85	15.25	9.90	70.68	16.93
TLLCM [20]	Trad	1.03	0.91	79.09	58.99	3.31	0.78	77.39	67.38
MDvsFA [20]	CNN	60.30	58.26	89.35	56.35	49.50	47.41	82.11	80.33
ACM [8]	CNN	72.33	71.43	96.33	9.33	60.97	58.02	90.58	21.78
AlcNet [10]	CNN	74.31	73.12	97.34	20.21	62.05	59.58	92.19	31.56
DNA-Net [10]	CNN	75.27	73.68	98.17	13.62	69.01	66.22	91.92	17.57
DCFR-Net [10]	CNN	76.23	74.69	99.08	6.52	65.41	65.45	93.60	7.35
AGPCNet [20]	CNN	70.60	70.16	97.25	37.44	62.82	63.01	90.57	29.82
Dim2Clear [20]	CNN	77.20	75.20	99.10	6.72	66.30	64.20	93.70	20.90
FC3-Net [20]	CNN	74.22	72.64	99.12	6.57	64.98	63.59	92.93	15.73
IAANet [20]	CNN-ViT	75.31	74.65	98.22	35.65	59.82	58.24	88.62	24.79
RKformer [20]	CNN-ViT	77.24	74.89	99.11	1.58	64.12	64.18	93.27	18.65
ISNet [20]	CNN	80.02	78.12	98.84	4.92	68.77	64.84	95.56	15.39
SegFormer [20]	ViT	76.01	66.43	96.35	35.83	60.12	57.23	89.22	18.47
TCI-Former [8]	CNN-ViT	80.79	79.85	99.23	4.19	70.14	67.69	96.31	14.81
MiM-ISTD [8]	Mamba	80.92	80.13	100.00	2.17	70.36	68.05	96.95	13.38
FDI-Net [8]	CNN-ViT	81.86	81.08	99.14	4.51	72.01	71.99	97.33	12.23
TAPM-Net (Ours)	Mamba	81.94	81.24	100.00	1.98	74.38	73.65	96.35	11.42

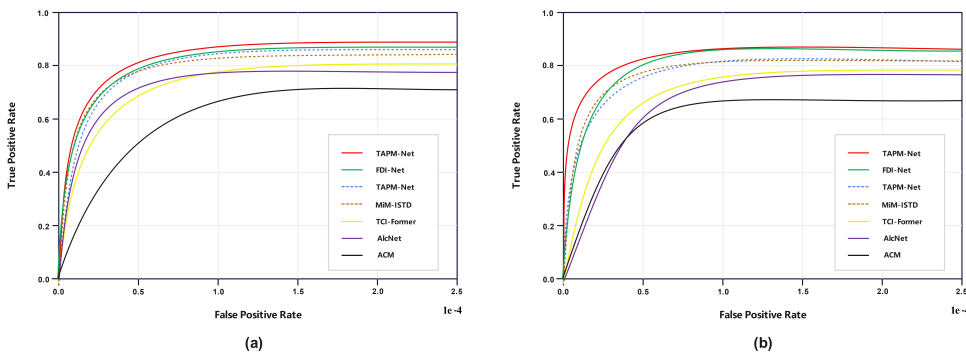


Figure 4: ROC curves of several methods on (a) NUAA-SIRST and (b) IRSTD-1k.

To analyze how TAPM-Net progressively refines target representations, Figure 6 depicts the multi-stage feature responses from the encoder (En-stage 1 to En-stage 4) and decoder (De-stage 3 to De-stage 1). The examples are selected from both NUAA-SIRST and IRSTD-1k datasets. As shown, the encoding stages gradually suppress background interference while enhancing the target response as the resolution decreases. The decoding stages progressively recover spatial details and refine the target regions towards the final prediction. These results show the complete transformation from raw inputs to features and then to accurate segmentation masks.

Ablation study. We assess the contribution of each component of TAPM-Net on NUAA-SIRST. Table 2 shows that PGM and TASB independently improve detection, and their joint use achieves the best performance. The results in Table 3 further confirm the effectiveness of PGM’s explicit trajectory modeling and feature fusion. Finally, Table 4 shows that

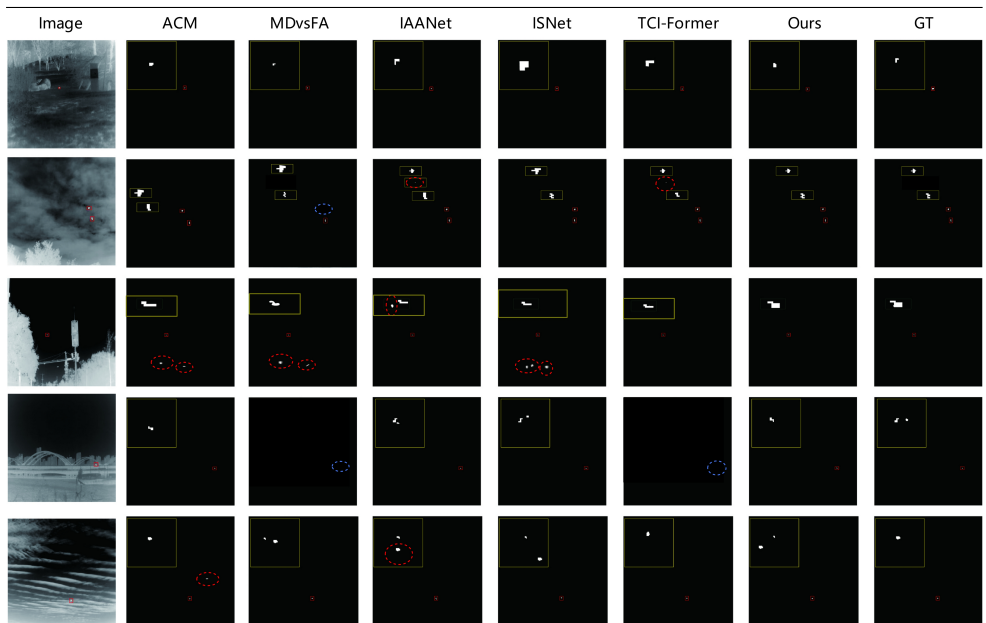


Figure 5: Visualization of results of different ISTD methods, where the GT column depicts the ground truth. Red boxes indicate target locations, yellow boxes indicate magnified prediction regions, red circles mark false alarms, and blue circles indicate missed detections.

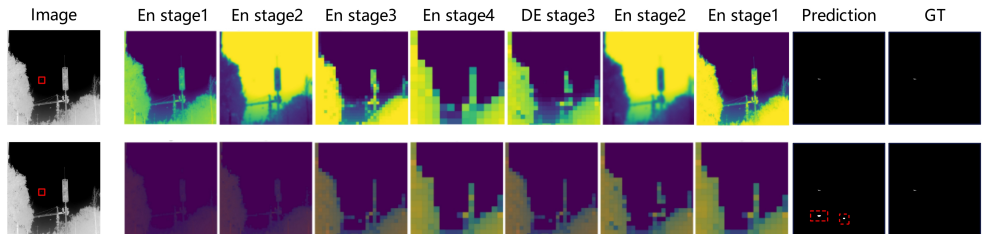


Figure 6: Feature responses from the encoder (En-stage 1 to En-stage 4) and de-encoder (De-stage 3 to De-stage 1). The first row corresponds to TAPM-Net, while the second one to TCI-Former. The GT column depicts the ground truth.

Mamba-based TASB outperforms standard residual and bottleneck blocks, demonstrating its advantage in capturing long-range spatial context and enhancing semantic consistency.

5 Conclusion

In this work, we proposed TAPM-Net, a new ISTD method that combines perturbation-guided feature modeling with Mamba-based state-space learning. TAPM-Net introduces a two-step process that first builds energy maps to guide feature extraction along trajectories and then models feature propagation along these trajectories to enhance target representation. TAPM-Net further aligns these features with multi-level visual embeddings to improve spatial consistency. Experimental results on NUAA-SIRST and IRSTD-1k show that TAPM-Net

Table 2: Performance of TAPM-Net on NUAA-SIRST when different components are removed.

Variant	IoU↑	nIoU↑	Pd↑	Fa↓
U-Net	63.12	66.56	91.23	43.23
U-Net+PGM	72.45	73.98	95.63	8.78
U-Net+TASB	74.98	76.12	98.26	6.45
U-Net+PGM+TASB (full)	81.04	80.24	100.0	1.98

Table 3: Performance of TAPM-Net on NUAA-SIRST with several variants of PGM.

Variant	IoU↑	nIoU↑	Pd↑	Fa↓
En. Map (only)	50.44	52.92	88.23	19.23
En. Map+Traj.	74.78	76.52	98.45	7.18
En. Map+Traj.+ Fusion (full)	81.04	80.24	100.0	1.98

Table 4: Performance of TAPM-Net on NUAA-SIRST with several variants of TASB.

Variant	IoU↑	nIoU↑	Pd↑	Fa↓
ResBlock	79.12	79.88	98.49	4.51
Bottle Neck	78.89	79.36	98.95	5.14
TASB (full)	81.04	80.24	100.0	1.98

achieves higher detection accuracy and lower false alarm rates compared to several methods, demonstrating its effectiveness for small target detection in complex infrared scenes.

References

- [1] Xiangzhi Bai and Fugen Zhou. Analysis of new top-hat transformation and the application for infrared dim small target detection. *Pattern Recognition*, 43(6):2145–2156, 2010.
- [2] Filipe De Avila Belbute-Peres, Thomas Economou, and Zico Kolter. Combining differentiable pde solvers and graph neural networks for fluid flow prediction. In *international conference on machine learning*, pages 2402–2411. PMLR, 2020.
- [3] Hu Cao, Yueyue Wang, Joy Chen, Dongsheng Jiang, Xiaopeng Zhang, Qi Tian, and Manning Wang. Swin-unet: Unet-like pure transformer for medical image segmentation. In *European conference on computer vision*, pages 205–218. Springer, 2022.
- [4] Tianxiang Chen, Qi Chu, Bin Liu, and Nenghai Yu. Fluid dynamics-inspired network for infrared small target detection. In *IJCAI*, pages 590–598, 2023.
- [5] Tianxiang Chen, Zhentao Tan, Qi Chu, Yue Wu, Bin Liu, and Nenghai Yu. Tci-former: Thermal conduction-inspired transformer for infrared small target detection. In *Proceedings of the AAAI Conference on Artificial Intelligence*, volume 38, pages 1201–1209, 2024.
- [6] Tianxiang Chen, Zi Ye, Zhentao Tan, Tao Gong, Yue Wu, Qi Chu, Bin Liu, Nenghai Yu, and Jieping Ye. Mim-istd: Mamba-in-mamba for efficient infrared small target detection. *IEEE Transactions on Geoscience and Remote Sensing*, 2024.
- [7] Yimian Dai and Yiquan Wu. Reweighted infrared patch-tensor model with both non-local and local priors for single-frame small target detection. *IEEE journal of selected topics in applied earth observations and remote sensing*, 10(8):3752–3767, 2017.

- [8] Yimian Dai, Yiquan Wu, Yu Song, and Jun Guo. Non-negative infrared patch-image model: Robust target-background separation via partial sum minimization of singular values. *Infrared Physics & Technology*, 81:182–194, 2017.
- [9] Yimian Dai, Yiquan Wu, Fei Zhou, and Kobus Barnard. Asymmetric contextual modulation for infrared small target detection. In *Proceedings of the IEEE/CVF winter conference on applications of computer vision*, pages 950–959, 2021.
- [10] Yimian Dai, Yiquan Wu, Fei Zhou, and Kobus Barnard. Attentional local contrast networks for infrared small target detection. *IEEE transactions on geoscience and remote sensing*, 59(11):9813–9824, 2021.
- [11] He Deng, Xianping Sun, Maili Liu, Chaohui Ye, and Xin Zhou. Small infrared target detection based on weighted local difference measure. *IEEE Transactions on Geoscience and Remote Sensing*, 54(7):4204–4214, 2016.
- [12] Zhiwen Deng, Chuangxin He, Yingzheng Liu, and Kyung Chun Kim. Super-resolution reconstruction of turbulent velocity fields using a generative adversarial network-based artificial intelligence framework. *Physics of Fluids*, 31(12), 2019.
- [13] Linyu Fan, Yingying Wang, Guoliang Hu, Feifei Li, Yuhang Dong, Hui Zheng, Changqing Lin, Yue Huang, and Xinghao Ding. Diffusion-based continuous feature representation for infrared small-dim target detection. *IEEE Transactions on Geoscience and Remote Sensing*, 62:1–17, 2024.
- [14] Chenqiang Gao, Deyu Meng, Yi Yang, Yongtao Wang, Xiaofang Zhou, and Alexander G Hauptmann. Infrared patch-image model for small target detection in a single image. *IEEE transactions on image processing*, 22(12):4996–5009, 2013.
- [15] Jinhui Han, Yong Ma, Bo Zhou, Fan Fan, Kun Liang, and Yu Fang. A robust infrared small target detection algorithm based on human visual system. *IEEE Geoscience and Remote Sensing Letters*, 11(12):2168–2172, 2014.
- [16] Tao Huang, Xiaohuan Pei, Shan You, Fei Wang, Chen Qian, and Chang Xu. Lo-calmamba: Visual state space model with windowed selective scan. *arXiv preprint arXiv:2403.09338*, 2024.
- [17] Boyang Li, Chao Xiao, Longguang Wang, Yingqian Wang, Zaiping Lin, Miao Li, Wei An, and Yulan Guo. Dense nested attention network for infrared small target detection. *IEEE Transactions on Image Processing*, 32:1745–1758, 2022.
- [18] Fanzhao Lin, Shiming Ge, Kexin Bao, Chenggang Yan, and Dan Zeng. Learning shape-biased representations for infrared small target detection. *IEEE Transactions on Multimedia*, 26:4681–4692, 2023.
- [19] Qiankun Liu, Rui Liu, Bolun Zheng, Hongkui Wang, and Ying Fu. Infrared small target detection with scale and location sensitivity. In *Proceedings of the IEEE/CVF Conference on Computer Vision and Pattern Recognition*, pages 17490–17499, 2024.
- [20] Jun Ma, Feifei Li, and Bo Wang. U-mamba: Enhancing long-range dependency for biomedical image segmentation. *arXiv preprint arXiv:2401.04722*, 2024.

- [21] Tianlei Ma, Zhen Yang, Yi-Fan Song, Jing Liang, and Heshan Wang. Dmef-net: Lightweight infrared dim small target detection network for limited samples. *IEEE Transactions on Geoscience and Remote Sensing*, 61:1–15, 2023.
- [22] Peiwen Pan, Huan Wang, Chenyi Wang, and Chang Nie. Abc: Attention with bilinear correlation for infrared small target detection. In *2023 IEEE International Conference on Multimedia and Expo (ICME)*, pages 2381–2386. IEEE, 2023.
- [23] Yao Qin, Lorenzo Bruzzone, Chengqiang Gao, and Biao Li. Infrared small target detection based on facet kernel and random walker. *IEEE Transactions on Geoscience and Remote Sensing*, 57(9):7104–7118, 2019.
- [24] Connor Schenck and Dieter Fox. Spnets: Differentiable fluid dynamics for deep neural networks. In *Conference on Robot Learning*, pages 317–335. PMLR, 2018.
- [25] Abdelrahman Shaker, Syed Talal Wasim, Salman Khan, Juergen Gall, and Fahad Shahbaz Khan. Groupmamba: Parameter-efficient and accurate group visual state space model. *arXiv preprint arXiv:2407.13772*, 2024.
- [26] Yuheng Shi, Minjing Dong, and Chang Xu. Multi-scale vmamba: Hierarchy in hierarchy visual state space model. *arXiv preprint arXiv:2405.14174*, 2024.
- [27] Heng Sun, Junxiang Bai, Fan Yang, and Xiangzhi Bai. Receptive-field and direction induced attention network for infrared dim small target detection with a large-scale dataset irdst. *IEEE Transactions on Geoscience and Remote Sensing*, 61:1–13, 2023.
- [28] Yang Sun, Jungang Yang, and Wei An. Infrared dim and small target detection via multiple subspace learning and spatial-temporal patch-tensor model. *IEEE Transactions on Geoscience and Remote Sensing*, 59(5):3737–3752, 2020.
- [29] Huan Wang, Luping Zhou, and Lei Wang. Miss detection vs. false alarm: Adversarial learning for small object segmentation in infrared images. In *Proceedings of the IEEE/CVF international conference on computer vision*, pages 8509–8518, 2019.
- [30] Kewei Wang, Shuaiyuan Du, Chengxin Liu, and Zhiguo Cao. Interior attention-aware network for infrared small target detection. *IEEE Transactions on Geoscience and Remote Sensing*, 60:1–13, 2022.
- [31] Ziyang Wang and Chao Ma. Weak-mamba-unet: Visual mamba makes cnn and vit work better for scribble-based medical image segmentation. *arXiv preprint arXiv:2402.10887*, 2024.
- [32] Tianhao Wu, Boyang Li, Yihang Luo, Yingqian Wang, Chao Xiao, Ting Liu, Jungang Yang, Wei An, and Yulan Guo. Mtu-net: Multilevel transunet for space-based infrared tiny ship detection. *IEEE Transactions on Geoscience and Remote Sensing*, 61:1–15, 2023.
- [33] Xin Wu, Danfeng Hong, and Jocelyn Chanussot. Uiu-net: U-net in u-net for infrared small object detection. *IEEE Transactions on Image Processing*, 32:364–376, 2022.
- [34] Xin Wu, Danfeng Hong, and Jocelyn Chanussot. Uiu-net: U-net in u-net for infrared small object detection. *IEEE Transactions on Image Processing*, 32:364–376, 2022.

- [35] Enze Xie, Wenhai Wang, Zhiding Yu, Anima Anandkumar, Jose M Alvarez, and Ping Luo. Segformer: Simple and efficient design for semantic segmentation with transformers. *Advances in neural information processing systems*, 34:12077–12090, 2021.
- [36] Hongyang Xie, Hongyang He, Boyang Fu, and Victor Sanchez. Grdt: Towards robust deepfake detection using geometric representation distribution and texture. In *Proceedings of the Winter Conference on Applications of Computer Vision*, pages 734–744, 2025.
- [37] Shoukui Yao, Yi Chang, and Xiaojuan Qin. A coarse-to-fine method for infrared small target detection. *IEEE Geoscience and Remote Sensing Letters*, 16(2):256–260, 2018.
- [38] Landan Zhang and Zhenming Peng. Infrared small target detection based on partial sum of the tensor nuclear norm. *Remote Sensing*, 11(4):382, 2019.
- [39] Landan Zhang, Lingbing Peng, Tianfang Zhang, Siying Cao, and Zhenming Peng. Infrared small target detection via non-convex rank approximation minimization joint 1 2, 1 norm. *Remote Sensing*, 10(11):1821, 2018.
- [40] Landan Zhang, Lingbing Peng, Tianfang Zhang, Siying Cao, and Zhenming Peng. Infrared small target detection via non-convex rank approximation minimization joint 1 2, 1 norm. *Remote Sensing*, 10(11):1821, 2018.
- [41] Mingjin Zhang, Haichen Bai, Jing Zhang, Rui Zhang, Chaoyue Wang, Jie Guo, and Xinbo Gao. Rkformer: Runge-kutta transformer with random-connection attention for infrared small target detection. In *Proceedings of the 30th ACM International Conference on Multimedia*, pages 1730–1738, 2022.
- [42] Mingjin Zhang, Qianqian Wu, Jing Zhang, Xinbo Gao, Jie Guo, and Dacheng Tao. Fluid micelle network for image super-resolution reconstruction. *IEEE Transactions on Cybernetics*, 53(1):578–591, 2022.
- [43] Mingjin Zhang, Ke Yue, Jing Zhang, Yunsong Li, and Xinbo Gao. Exploring feature compensation and cross-level correlation for infrared small target detection. In *Proceedings of the 30th ACM International Conference on Multimedia*, pages 1857–1865, 2022.
- [44] Mingjin Zhang, Rui Zhang, Yuxiang Yang, Haichen Bai, Jing Zhang, and Jie Guo. Isnet: Shape matters for infrared small target detection. In *Proceedings of the IEEE/CVF conference on computer vision and pattern recognition*, pages 877–886, 2022.
- [45] Tianfang Zhang, Lei Li, Siying Cao, Tian Pu, and Zhenming Peng. Attention-guided pyramid context networks for detecting infrared small target under complex background. *IEEE Transactions on Aerospace and Electronic Systems*, 59(4):4250–4261, 2023.
- [46] Tianfang Zhang, Lei Li, Siying Cao, Tian Pu, and Zhenming Peng. Attention-guided pyramid context networks for detecting infrared small target under complex background. *IEEE Transactions on Aerospace and Electronic Systems*, 59(4):4250–4261, 2023.